










## Seafloor earthquake ruptures and mass wasting from the 2004 $M_w$ 6.3 Les Saintes submarine earthquake

Alex Hughes <sup>1✉</sup>, Javier Escartín<sup>2</sup>, Jeremy Billant<sup>3</sup>, Frédérique Leclerc <sup>3</sup>, Muriel Andreani <sup>4</sup>, Jean-Arthur Olive <sup>2</sup>, Aurélien Arnaubec <sup>5</sup>, Alexandre Dano<sup>3</sup>, Arthur Delorme<sup>1</sup>, Christine Deplus <sup>1</sup>, Nathalie Feuillet <sup>1</sup>, Caroline Gini <sup>6</sup>, Nuno Gracias<sup>7</sup>, Cédric Hamelin<sup>8</sup>, Klemen Istenič<sup>7</sup>, Jean-Christophe Komorowski <sup>1</sup>, Anne Le Friant<sup>1</sup>, Claire Marchand<sup>9</sup>, Catherine Mével<sup>1</sup>, Solveig Lie Onstad<sup>10</sup> & Xavier Quidelleur<sup>11</sup>

The seismic hazard posed by submarine faults and the capacity of submarine earthquakes to trigger mass wasting are poorly understood because we lack detailed characterizations of coseismic ruptures at the seafloor. Here, we present comprehensive mapping of a seafloor rupture caused by the 2004  $M_w$  6.3 Les Saintes earthquake on the Roseau normal fault in the Lesser Antilles. We report the visual characteristics, displacement profile, and note pronounced asymmetry of the rupture that bears similarities with well-studied subaerial normal fault ruptures. We also identify footwall-derived mass wasted debris that locally cover the coseismic rupture, and show that ground accelerations of 0.1–0.2 g can trigger submarine mass wasting events in well consolidated bedrock along unstable, over-steepened, scarps. Our study demonstrates the potential of underwater vehicles for detailed mapping of seafloor ruptures and hints at a key role for earthquakes in shaping submarine bedrock landscapes by triggering mass wasting events.

<sup>1</sup> Université Paris Cité, Institut de Physique du Globe de Paris, CNRS, F-75005 Paris, France. <sup>2</sup> Laboratoire de Géologie, Ecole Normale Supérieure (CNRS UMR 8538), PSL Research University, Paris, France. <sup>3</sup> Université Côte d'Azur, CNRS, Observatoire de la Côte d'Azur, IRD, Valbonne, France. <sup>4</sup> Laboratoire de Géologie de Lyon, Université de Lyon, ENS de Lyon, CNRS, UMR 5276 LGL-TPE, 69622 Villeurbanne, France. <sup>5</sup> IFREMER, Ctr Mediterranee, Unité Syst. Marins, CS 20330, F-83507 La Seyne Sur Mer, France. <sup>6</sup> Department of Earth Sciences, Memorial University of Newfoundland, St John's, NL, Canada. <sup>7</sup> Computer Vision and Robotics Institute, University of Girona, Girona, Spain. <sup>8</sup> Independent Scholar, Søndre Skogveien 7, 5055 Bergen, Norway. <sup>9</sup> Sea Operations Division, iXblue, 6 Quai François Mitterrand, NEF XX, 13600 La Ciotat, France. <sup>10</sup> University of Bergen Centre for Deep Sea Research, Bergen, Norway. <sup>11</sup> Université Paris-Saclay, CNRS, GEOPS, Orsay 91405, France. ✉email: [dralexhughes84@gmail.com](mailto:dralexhughes84@gmail.com)

Mapping coseismic offsets of the Earth's surface provides valuable insight into the dynamics of the underlying rupture and helps to quantify earthquake hazards. Rupture data from terrestrial normal faults have been used to assemble scaling relationships between earthquake slip, moment, and source dimension<sup>1,2</sup>, to ground truth geophysical models of slip distributions<sup>3,4</sup>, and to infer the associated static stress transfers<sup>5–7</sup>. Underwater, high-resolution seafloor mapping is challenging, and existing submarine observations of coseismic ruptures are typically incomplete and rare<sup>8–11</sup> and thus insufficient to inform scaling relationships or assess seismic risk. Previous work suggests that submarine ruptures may generate surface offsets larger than subaerial ruptures of comparable source characteristics due to the specific environmental and rheological conditions<sup>10</sup>. For example, fault lubrication from near-surface fluids could enhance surface rupture propagation<sup>12</sup> or, in deeper water, pressure from the overlying water column could promote shear failure at the seafloor<sup>13</sup>. Moreover, heterogeneous seafloor displacement is a key control on modeled tsunami height distributions<sup>14–17</sup>, but tsunami propagation models usually rely on rupture profiles inferred from geophysical or geodetic models that lack ground-truthing from seafloor observations<sup>15,17</sup>. Detailed characterizations of seafloor ruptures are therefore needed to test these hypotheses and help assess the specific hazards posed by submarine faults.

Submarine mass wasting is a widespread process that may be facilitated, or triggered by, reduced internal friction associated with fluid circulation, fluidification of sediments, or alteration weakening<sup>18–20</sup>. Ground accelerations from earthquakes are also an important mass wasting trigger in active terrestrial settings<sup>21,22</sup>, in fjords<sup>23,24</sup>, and offshore in sediments along continental slopes<sup>20,25–27</sup>. Historically, the characteristics of paleoseismic seafloor events are indirectly inferred from seismically triggered turbidites in sediment cores<sup>28</sup>. However, evaluating the level of earthquake-induced ground accelerations required to trigger submarine mass wasting events (triggering thresholds) has also proved difficult because pre- and post- earthquake seafloor surveys are rare, and we lack sufficient examples of seafloor earthquake ruptures that can be directly linked to specific mass wasting events<sup>26,27</sup>. On the deep ocean floor, the dominant morphological features are volcanic abyssal hills dissected and tilted by seismically active normal faults<sup>29,30</sup>. Therefore, establishing triggering thresholds and links between submarine earthquakes and mass wasting is not only important from a hazard perspective, but will also help understand how tectonics and surface processes interact over geological time to shape the morphology of the global seafloor.

The Roseau fault (Lesser Antilles) is an ideal setting to investigate seafloor earthquake ruptures and links between submarine earthquakes and mass wasting. The Roseau fault is a northeast-dipping normal fault that runs northwest–southeast for ~40 km, bounding an active extensional half-graben within the Lesser Antilles volcanic arc<sup>3,13</sup> (Fig. 1a). The fault has five previously mapped segments (Sec Pate, Canyon, Roseau, Le Havre, Colibri; Fig. 1) and exhibits a pronounced fault scarp reaching a maximum height of ~170 m along the Roseau segment<sup>13,30</sup>. The 2004  $M_w$  6.3 Les Saintes earthquake had its hypocenter at ~10 km depth on the Roseau fault and was followed by six large aftershocks ( $M_w$  4.8–5.8)<sup>3,31,32</sup>. The earthquake also triggered a tsunami with run-up heights of 2 m along the coast of the Les Saintes islands<sup>14</sup>. Geophysical inversion models for the Les Saintes earthquake predicted a maximum of 0.6–0.9 m of coseismic seafloor displacement during the 2004  $M_w$  6.3 main shock<sup>3,32</sup>. The predicted seafloor breaching was confirmed by observations and mapping with a remotely operated vehicle (ROV) during the 2013 ODEMAR cruise<sup>33</sup>, which documented a 0.9 m high ribbon

of coseismically exposed bedrock at the base of the Roseau fault scarp<sup>10</sup>. ROV observations also showed mass wasted debris from the footwall that locally covered the coseismic ribbon and indicated that active mass wasting occurred either during or after the 2004 earthquake<sup>10</sup>.

These initial observations were limited to ~3 km along the base of the Roseau fault, while geophysical models predicted 10 km of surface rupture during the 2004 main shock<sup>3,32</sup>. This left much of the potential surface rupture of the Les Saintes earthquake unmapped. Here, we present data from the 2017 SUBSAINTES cruise<sup>34</sup> where we investigated the Roseau fault scarp and the 2004 coseismic rupture with an ROV and an autonomous underwater vehicle (AUV). We present a comprehensive coseismic rupture profile for a submarine normal fault and combine qualitative observations of the rupture and local mass wasting with maps of peak ground accelerations derived from local seismicity catalogs. This work provides a blueprint for mapping submarine earthquake ruptures and demonstrates that earthquake-induced ground accelerations of 0.1–0.2 g can trigger mass wasting in well consolidated bedrock.

## Results

**The Les Saintes earthquake rupture.** We used high-resolution, near-bottom AUV bathymetry, ROV video imagery, and scaled and georeferenced 3D terrain models of selected fault outcrops to map the 2004 earthquake rupture (see Methods)<sup>35,36</sup>. These data show variations of along-fault rupture style while providing quantitative constraints on rupture displacement.

The fault's surface expression and the coseismic rupture are most pronounced along the Roseau segment where the fault scarp exposes basement including a lava flow dated to  $4.12 \pm 0.06$  Ma<sup>37</sup>. The free face is clearly visible at the base of the scarp in 3D models and video imagery where it comprises a planar, sub-vertical surface coated by a dark manganese patina (Fig. 2a–c). Above the free face, the scarp is eroded and forms a blocky, discontinuous, surface covered with small amounts of rubble and sediment (Fig. 2b). The free face reaches a maximum height of ~50 m<sup>30</sup> and often displays a ribbon of smooth rock at its base that is generally smoother than the overlying rock and lacks the manganese patina (Fig. 2a–d). This ribbon is reminiscent of subaerial coseismic ruptures<sup>38,39</sup> and was previously interpreted as fresh rock exposed by coseismic slip during the 2004 Les Saintes earthquake at just one location (model 20: Supplementary Data 1)<sup>10</sup>. We mapped the coseismic ribbon continuously for more than 4 km along strike of the Roseau segment (Fig. 3), which confirms the ribbons coseismic nature and documents efficient localization of the rupture along the Roseau segment.

The expression of the surface rupture varies along strike and in different lithology (Fig. 2), in particular, along the northwest and southeast sections of the Roseau fault. Towards its southeast tip, the Roseau fault branches out into several distributed fault strands where it dissects the Roseau volcano (Fig. 1c). Here, the complex fault geometry precludes a systematic and exhaustive seafloor exploration along all faults and rupture observations are sparse (Fig. 3). Consequently, towards the southeast tip, we only identified the coseismic ribbon in four locations covering ~8 km along strike. The northwest end of the fault cuts a series of submarine canyons along the southwest slope of the Les Saintes Plateau (Fig. 1b), within a mixture of consolidated and unconsolidated sediment and rubble that paves the seafloor. Coseismic ruptures in this area lack the clear ribbons observed on basement fault outcrops in the Roseau segment, and instead exhibit small scarps or extensional fissures through the sediment and rubble cover (Fig. 2e–i).

We measured vertical seafloor displacement using both laser calipers and directly from 3D outcrop models (Fig. 3;

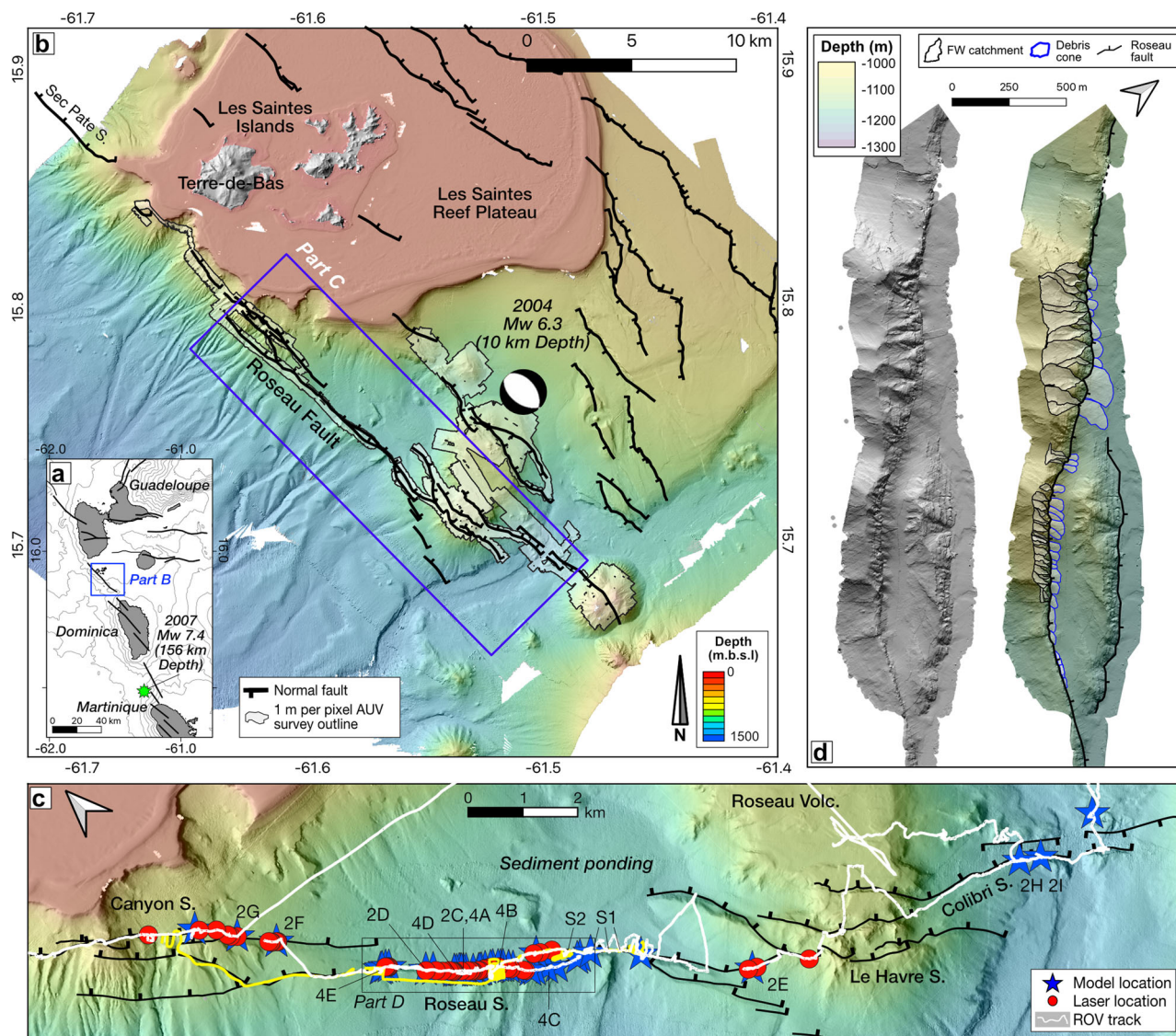


**Fig. 1 Study location.** **a** Regional map of the Lesser Antilles showing the location of the study area. The green star shows the epicenter of a  $M_w$  7.4 earthquake in 2007. **b** Map of the Roseau fault and the Les Saintes islands based on 10-m per pixel regional bathymetry. Faults are from ref. <sup>13</sup> and epicenter of the Les Saintes earthquake is shown by the beachball<sup>3</sup>. **c** Close up view of the study area showing remotely operated vehicle tracks from 2013 ODEMAR cruise (yellow) and 2017 SUBSAINTES cruise (white) and the location of 3D outcrop models and laser measurements. The labels show the location of models in Figs. 2 and 4 and the photos in Supplementary Figs. 1–2. **d** Near-bottom bathymetry from the Roseau segment showing the location of footwall (FW) catchments and associated debris cones on either side of the Roseau fault<sup>30</sup>. ROV Remotely operated vehicle.

Supplementary Data 1–5; see Methods). The coseismic rupture spans 18 km along the Roseau fault scarp (Fig. 3), which extends the previously identified ~3 km rupture and significantly exceeds the 10 km predicted by geophysical models<sup>3,32</sup>. Coseismic vertical displacement shows a distinct northwest skew along strike to form an asymmetric displacement profile with ~0.6 m average vertical displacement (Fig. 3). We record a maximum coseismic vertical displacement of 2.7 m towards the northwest end of the rupture, which tapers to 0.1 m northwestward and to <0.5 m southeastwards (Fig. 3).

The maximum displacement of 2.7 m significantly exceeds that predicted by seismic inversion models, which indicated a maximum of 0.6–0.9 m of coseismic seafloor offset and 1.8 m of subsurface slip<sup>3</sup> (Fig. 3d). This discrepancy may be partially attributed to free surface effects near the seafloor, which could promote surface slip due to a reduction in near-surface elastic resistance<sup>40–42</sup>. Distributed or off-fault deformation<sup>43,44</sup> and

gravity driven processes<sup>45</sup> can also affect the ratio of measured surface slip to slip inferred on the fault plane at depth. Off-fault deformation near the Roseau fault scarp includes pervasive cracks of sedimented seafloor at the base of the scarp that extend ~200 m away from the fault trace into the hanging wall (Supplementary Fig. 1) as well as possible antithetic scarps dissecting these sediments (Supplementary Fig. 1d). However, the northwest-dip of the fault faces against the southeast-dipping regional slope and the basement is well lithified, neither of which are conducive to gravity driven processes locally increasing measured slip. Furthermore, redistribution of unconsolidated sand by bottom currents at the scarp base may account for local over- and underestimation in measured displacement.

The measured 2.7 m maximum vertical displacement may also reflect some component of displacement from the six largest aftershocks ( $4.8 < M_w < 5.8$ ). Tsunami modeling indicates that a vertical displacement of 2.5–3.5 m is required to match observed

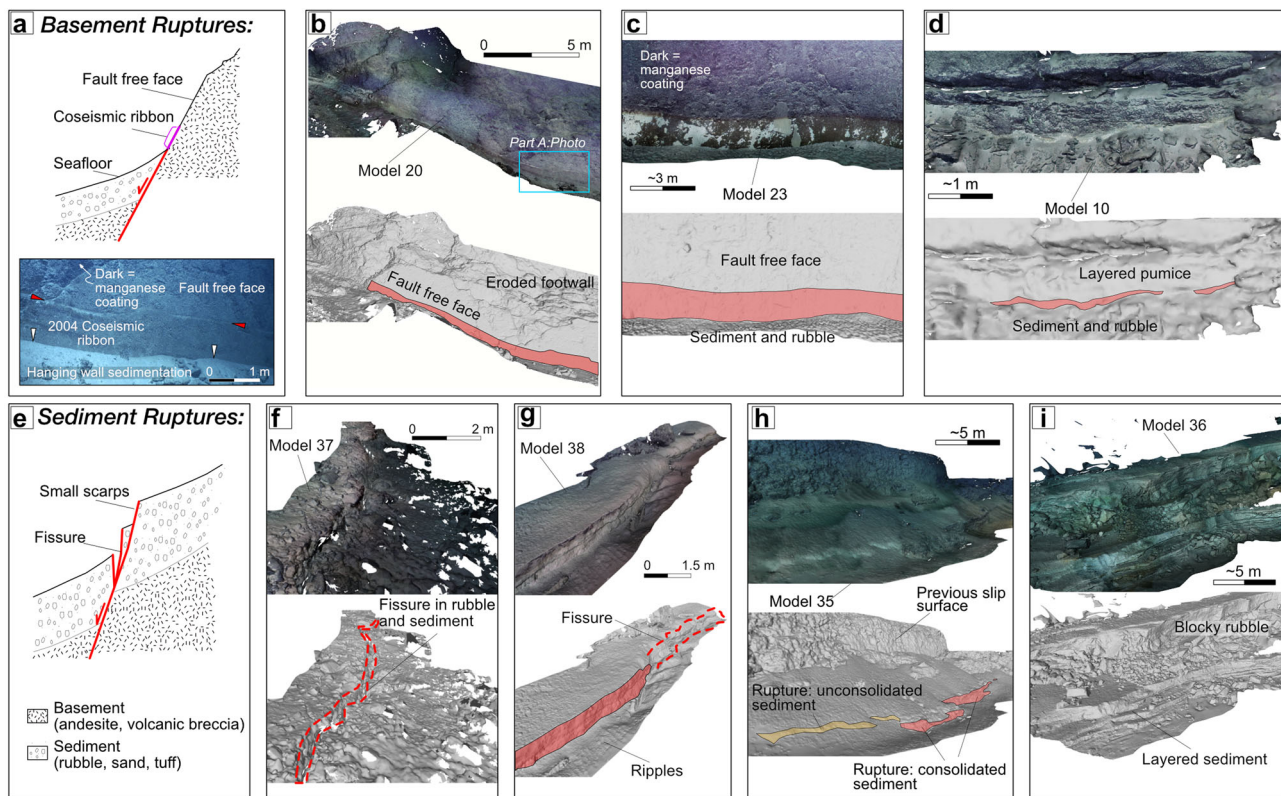


**Fig. 2 Rupture styles from the 2004 Les Saintes earthquake.** Schematic diagrams demonstrating contrasting ruptures styles in basement (**a**) versus sediment (**e**). The inset screenshot in part (**a**) is from remotely operated vehicle video footage showing a characteristic example of the 2004 rupture plane. Red arrows show the top of the rupture and white arrows denote the hanging wall cut-off. **b-d/f-i** Video-derived, 3D outcrop models showing coseismic rupture features associated with the 2004 earthquake. The upper images are color interpretations and the lower images are shaded models overlain with interpretation and annotations. The extent of the coseismic ribbon from the 2004 rupture is highlighted in red on the shaded models and the outline of fissures are shown with dashed red lines. For model details refer to the model number in Supplementary Data 1. **b-d** Ruptures in volcanic lithology. **f-i** Small scarps and fissures in sediment. The location of each model is in Fig. 1c.

tsunami amplitudes<sup>14</sup>, consistent with our rupture observations (Fig. 2). Conversely, simulations based on predicted seafloor displacements of 0.6 m inferred from seismic inversion models produce much smaller wave heights than those observed<sup>14</sup>. The outcome that the tsunami models require the  $M_w$  6.3 main shock to be associated with vertical displacements >2.5 m indicates that limited displacement occurred during the aftershock sequence.

**Mass wasting features and links to coseismic structures.** Mass wasting is ubiquitous along the Roseau fault scarp and fundamentally linked to its long-term morphological evolution<sup>10,13,30</sup>. A series of canyons and channels up to 200 m deep drain the southwest flank of the Les Saintes reef plateau<sup>13</sup> (Fig. 1b). Along the Roseau segment, surface uplift of the northeast-dipping Roseau fault has cut-off these regional channels and caused sediment ponding in the hanging wall<sup>13</sup> (Fig. 1c). Consequently, the scarp along the Roseau segment is mostly isolated from regional sedimentation and turbidity currents. Likewise, parts of the Colibri and Le Havre segments are on a bathymetric high created by the Roseau volcano and also isolated from regional sedimentation (Fig. 1c). In these isolated fault scarps, sediment inputs are limited to pelagic or hemipelagic sedimentation, in addition to local mass wasted debris from the footwall<sup>30</sup>. Pelagic sediments form a patchy and thin veneer (a few cm) along the footwall that blankets volcanic basement and rubble. The rubble concentrates along footwall catchments that funnel rubble and sediment towards debris cones at the foot of the scarp<sup>30</sup> (Fig. 1d),

thus providing the ideal sites to examine local mass wasting sourced from the footwall and their interactions with the fault.

Mass wasted rubble and sediment sourced from the footwall locally incise or cover the fault free face and the coseismic ribbon (Fig. 4). The coseismic ribbon often tapers towards channel outlets where it is covered by rubble sourced from the footwall (Fig. 4a–c). Away from catchment outlets, rubble and sediment mounds at the base of the scarp, up to 10–20 m wide and 2 m high, partially or fully cover the coseismic ribbon (Fig. 4d–e). The mass wasted debris covering the rupture clearly postdates the coseismic ribbon, with deposition that may be coseismic, postseismic, or a combination of both. To help ascertain when the mass wasting occurred, we surveyed overlapping sections of the Roseau fault in 2013 and 2017 with vertical imaging to construct overlapping photomosaics along ~4 km of the fault trace and covering a total area of ~73,000 m<sup>2</sup> (Figs. 3a, 5a). The overlapping surveys also cover catchment outlets, where mass wasted rubble is concentrated at the apex of debris cones (Fig. 1d)<sup>30</sup>. This location makes the overlapping photomosaics ideal to document mass transport and deposition over the 3.5-year inter-survey period, albeit well after the 2004 earthquake.

Systematic and comprehensive visual inspection of the 2013 and 2017 photomosaics, with identification of matching features at cm-scale (e.g., pebbles), reveal no identifiable changes in the position and distribution of rock debris and rubble during the 2013–2017 inter-survey period (Fig. 5). The only documented change in seafloor structure are ripples associated with mobile sediments. These are attributable to bottom currents, estimated at

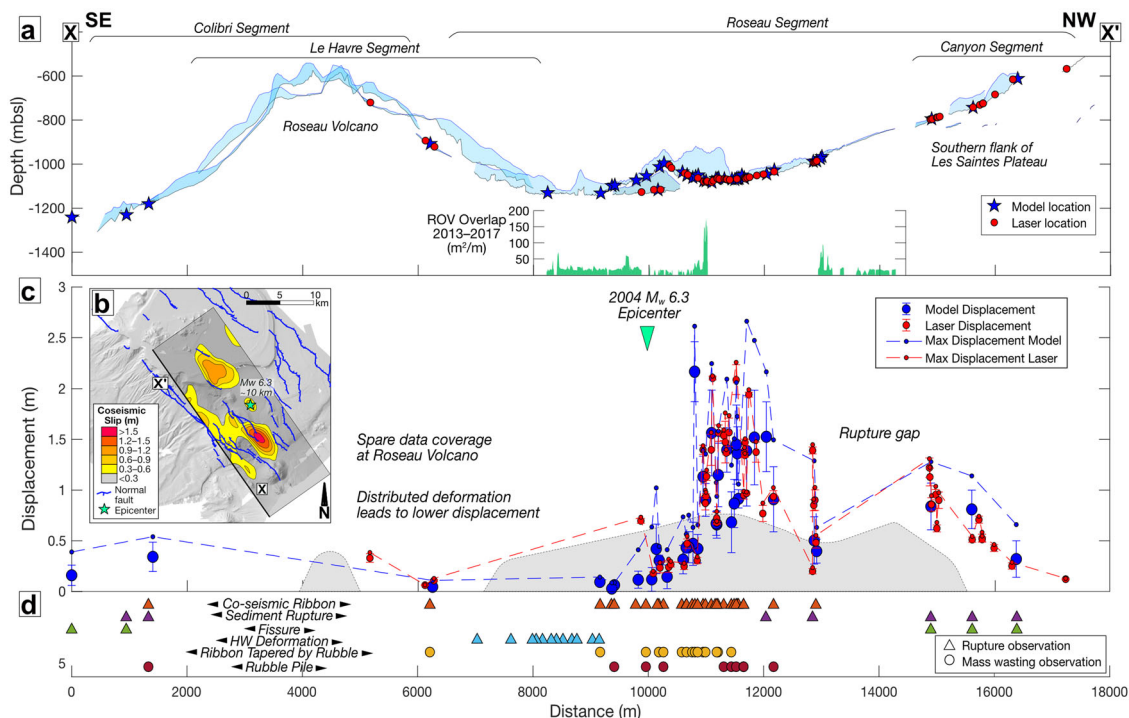


**Fig. 3** Seafloor rupture data. **a** Bathymetric profiles showing the height of the Roseau fault scarp along strike in pale blue and the location of 3D models and laser measurements. The green bar chart shows the overlap in remotely operated vehicle photomosaic coverage from surveys in 2013 compared to 2017. **b** Shaded relief map of the study area (same area as Fig. 1b) showing the surface projection of the slip at depth during the 2004 Les Saintes earthquake amended from ref. <sup>3</sup>. The gray rectangle is the fault outline used in the inversion models and the points X-X' show the projection line for parts (a, c, and d). **c** Along-strike coseismic vertical displacement measured from 3D models and with a laser caliper based on data in Supplementary Data 2, 3. The gray polygon shows surface slip from geophysical inversion models<sup>3</sup>. All error bars are one standard deviation. **d** The along-strike location of mass wasting or coseismic rupture observations based on data in Supplementary Data 5.

~0.5 m/s from ROV navigation, that are too weak to mobilize pebbles or trigger mass-wasting of rubble along the fault scarp. Along the Roseau segment, we identified one ~2 m<sup>2</sup> patch of rippled sediment in 2013 with exposed rubble in 2017. This rubble patch could result from mass wasting between 2013 and 2017 or from mobilized sediment exposing previously buried rubble (Supplementary Fig. 2). Even if this area corresponds to newly deposited rubble, this is the sole example of mobilization of coarse material between 2013 and 2017 that we identified.

## Discussion

**Implications for submarine seismic hazard.** The coseismic rupture profile presented here provides a unique opportunity to compare a submarine normal fault rupture with subaerial ruptures to inform aspects of earthquake behavior and provide inputs for seismic hazard analysis. When compared to data from a compilation of normal fault earthquakes (Supplementary Data 6), the surface rupture length (SRL) and maximum displacement ( $D_{\max}$ ) for the Les Saintes earthquake are within the range recorded for other normal fault earthquakes of a similar magnitude, albeit towards the upper end of the range with a large spread in the data (Fig. 6a, b). The along-strike distribution of surface rupture is similar to the  $M_w$  6.5 2016 Norcia earthquake in Italy (Depth: ~8 km, SRL: 22 km,  $D_{\max}$ : 2.1 m)<sup>38,39</sup> and the  $M_w$  6.9 1983 Borah Peak earthquake in northwestern USA (Depth: 16 km, SRL: 35 km,  $D_{\max}$ : 2.7–3.0 m)<sup>46,47</sup> and all three earthquakes show distinct asymmetry in the rupture profile with a pronounced skew towards one end of the rupture (Fig. 6c). Asymmetrical or skewed coseismic rupture profiles are common in subaerial faults and attributed to structural barriers or discontinuities<sup>48–50</sup>, fault bends at depth<sup>51</sup>, the varying size of off-

fault damage zones<sup>43,44</sup>, or the fault growth history<sup>52</sup>. Furthermore, zones of distributed deformation at fault tips can indicate fault propagation and termination towards the distributed deformation<sup>51,53</sup>. The complex fault network at the southeast tip of the Roseau fault could therefore indicate that the fault is propagating southeastwards<sup>13</sup>. This would partially explain the north-west-skew in the rupture profile because maximum slip often occurs on the section of fault farthest away from the fault-propagation direction<sup>54</sup>.

The submarine rupture profile from the Les Saintes earthquake provides an opportunity to test empirical earthquake scaling relationships on a submarine fault. Using the range of regressions for normal faults<sup>1</sup>, SRL is considered the most reliable predictor of moment magnitude ( $M_w$ )<sup>38</sup>. The SRL of 18 km measured here corresponds to an earthquake of  $M_w$  5.8–7.2 (Supplementary Data 7), which overlaps with the  $M_w$  6.3 2004 Les Saintes main shock<sup>3</sup>. However, standard regressions of earthquake magnitude versus rupture parameters do not account for the large spread in the data and do not capture fault properties like segmentation or maturity<sup>52</sup>. Surface rupture during the 2004 Les Saintes earthquake occurred mainly on the Roseau, Le Havre, and Colibri segments with minor surface displacement in the relay zone between the Roseau and Canyon segments (Fig. 3). This pattern of surface displacements is consistent with the modeled rupture at depth which has two main slip patches beneath the Roseau and Colibri segments (Fig. 3d). The Le Havre segment is not a major distinct fault segment, but rather a complex zone of diffuse, left-stepping, echelons in the relay zone between the Roseau and Colibri segments. That means the 2004 main shock ruptured two primary segments which is accordant with model predictions and empirical relations for structurally immature terrestrial faults<sup>55</sup>

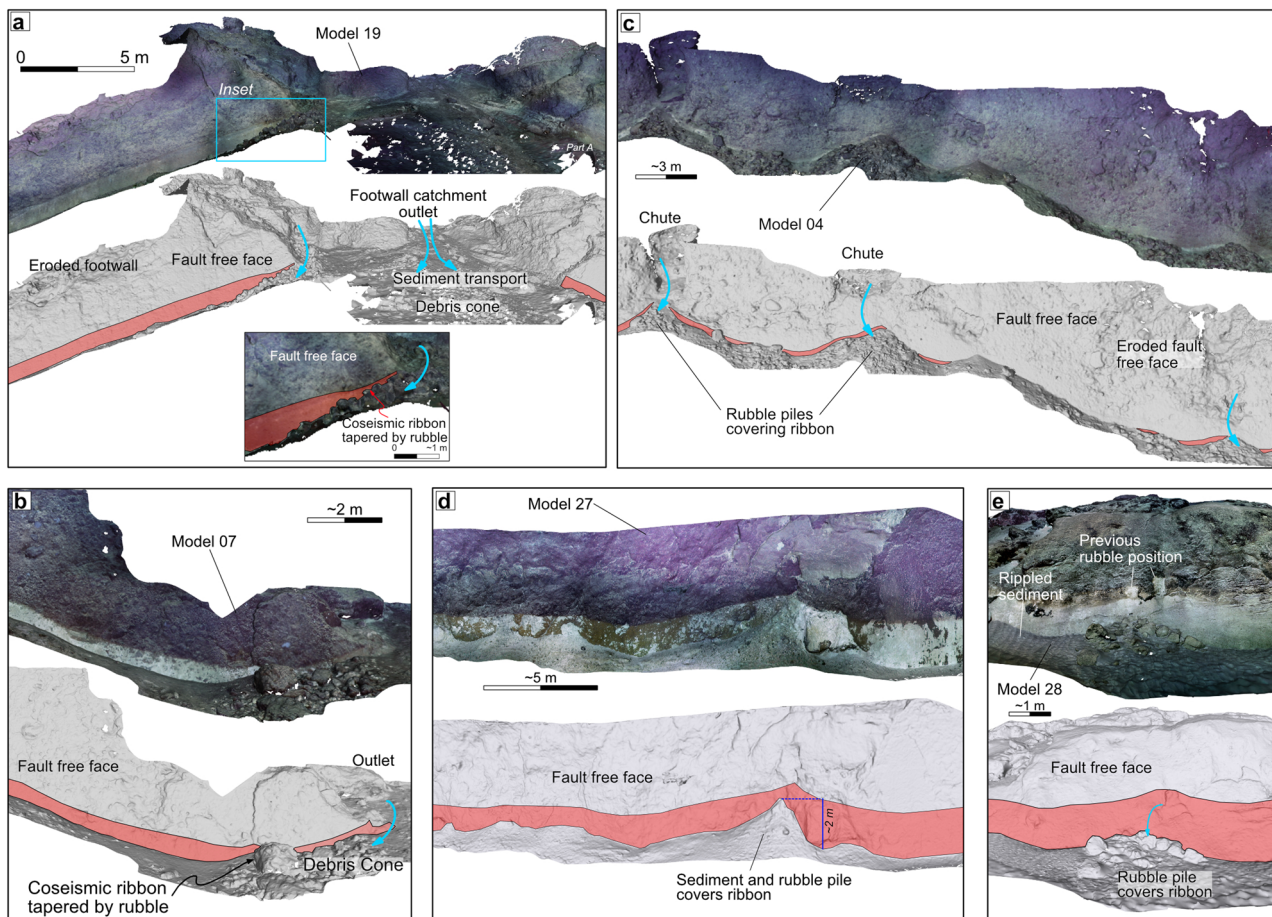


**Fig. 4** Mass wasting deposits covering the coseismic ribbon. **a–e** Video-derived, 3D outcrop models. In each example, the upper image is a texture-mapped 3D model and the lower one is a shaded model overlain with interpretation and annotations. The extent of the 2004 coseismic rupture is highlighted in red on the lower image. **a, b** Models located at the outlet of footwall catchments. Note how the ribbon tapers towards the crest of the rubble piles indicating that rubble sourced from the catchments postdates the ribbon. **c–e** Rubble and sediment piles covering the coseismic ribbon at the base of the fault free face away from catchment outlets. The blue arrows denote sediment/rubble transport. For model details refer to the model number in Supplementary Data 1 and the location of each model is shown in Fig. 1c.

(Fig. 6d). A structurally immature Roseau fault is consistent with the faults slow slip rate (0.15–0.40 mm/yr), limited total offset (450 m), and relatively young age (probably <3 Ma)<sup>13</sup>.

The general agreement of various rupture parameters for the Les Saintes earthquake with existing scaling relationships suggests consistency between surface rupture behavior for subaerial versus submarine faults. However, while we identified sediment cracks and possible antithetic scarps at distances up to 200 m away from the fault (Supplementary Fig. 1), the limited field of vision during ROV surveying and the lack of landscape view precludes comprehensive mapping of the width of the damage zone. Quantifying the damage zone is important because mass wasting may be focused within heavily fractured areas<sup>56</sup> and off-fault deformation can account for a large proportion of overall strain during normal fault earthquakes<sup>47</sup>.

**Linking earthquakes and mass wasting.** In several locations along the 2004 coseismic rupture, we observe rubble and sediment sourced from footwall catchments covering the coseismic ribbon (Fig. 4). This overlapping relationship clearly documents mass wasting that postdates the 2004 earthquake and aftershock sequence. The key question is whether the rubble was mobilized and transported downslope as a result of ground shaking during the 2004 earthquake, or results from a continuous shedding of material along the scarp due to processes like weathering or

sediment accumulation that result in stochastic mass wasting events unrelated to earthquakes.

On land, seismically triggered mass wasting is attributed to peak ground accelerations (PGA) during earthquakes, with shear stresses overcoming frictional forces to destabilize rock masses<sup>57</sup>. PGA is controlled by numerous parameters, including epicentral distance, magnitude, or the nature of the substrate and its frictional properties<sup>57–59</sup>. To calculate maps of PGA on the Roseau fault, we used local seismicity catalogs by the Centre de Données Sismologiques des Antilles and the Observatoire Volcanologique et Sismologique de Martinique and Guadeloupe<sup>60</sup> (see Methods). We used the spatial and temporal distribution of seismicity to predict maximum horizontal PGA for the study area over periods defined by the 2004 earthquake and repeat surveys of the seafloor in 2013 and 2017. The Roseau Fault was seismically quiescent prior to the 2004  $M_w$  6.3 earthquake (Fig. 7a, Supplementary Fig. 3), with a recurrence time for  $M_w \sim 6$  events estimated at several hundred to a few thousand years<sup>10</sup>. Following the  $M_w$  6.3 2004 main shock and six largest aftershocks, a slight spike in seismic activity is followed by a gradual decrease and leveling off after ~1000 days to a background level that persists today and that includes the 3.5-year inter-survey period (Fig. 7a, b).

Maximum horizontal PGA reached 0.24 g on the Roseau fault scarp during the period from the 2004 main shock to the 2013 ODEMAR cruise (Fig. 7d; Supplementary Data 8). For other

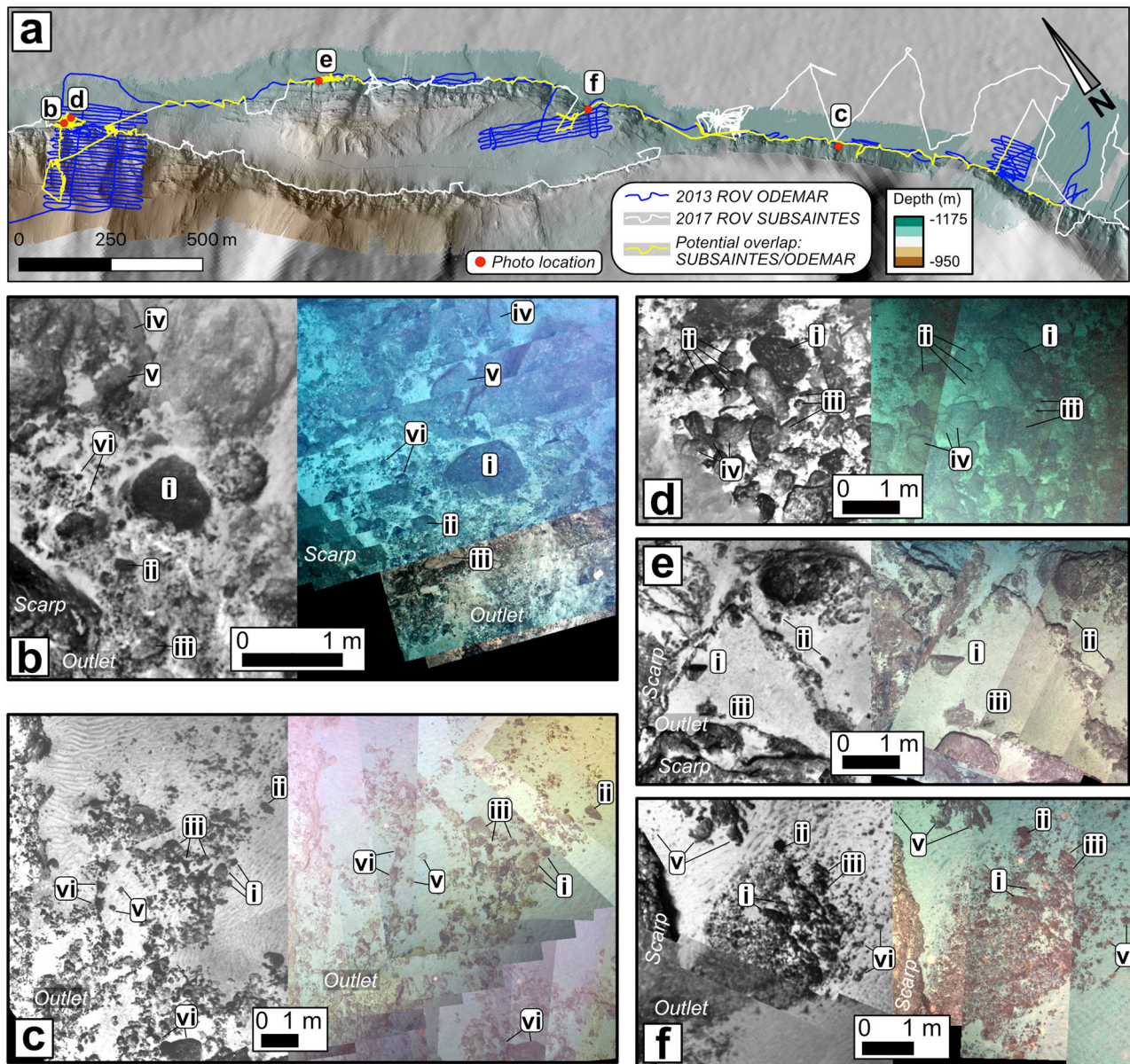


**Fig. 5 Comparison of rubble locations from 2013 to 2017.** **a** Map showing the tracks of the remotely operated vehicle (ROV) dives from the 2013 ODEMAR and 2017 SUBSAINTES cruises, areas of potential overlap between the two dives, and the location of the comparisons in parts **(b–f)**. Map location is the same as Fig. 1d. **b–f** Photomosaics comparing the distribution of mass-wasted sediments at the same location at catchment outlets from the ODEMAR cruise in 2013 (black and white)<sup>76</sup> with the SUBSAINTES cruise in 2017 (color)<sup>77</sup>. The Roman numerals point to several examples of cobbles/boulders which are in the same location in 2013 as in 2017. In all examples, there is some variation in the distribution of sand-sized sediment moved by bottom currents but little change in the distribution of cobbles or boulders.

periods (pre-shock, 2013–2017, and post 2017; Fig. 7c, e, f) maximum PGA on the Roseau fault are several orders of magnitude lower ( $<0.01$  g) and are most likely below the threshold to trigger mass wasting<sup>61</sup>. In terms of individual earthquakes, maximum PGA within the period from the 2004 earthquake to the 2013 cruise occurred during the main shock when horizontal PGA on the Roseau fault reached 0.24 g (Fig. 7g). The only other notable shaking event occurred during the largest aftershock of  $M_w$  5.8 on 14th February 2005 when PGA on the Roseau fault reached 0.12 g (Fig. 7i). These PGA values support a mobilization of material and its deposition immediately following the main shock and possibly the largest aftershock. From 2004 to 2017, the only other major earthquake in the area was a 2007  $M_w$  7.4 earthquake, 20 km offshore Martinique and at 156 km depth along the subduction plane (Fig. 1a). With a calculated PGA of up

to 0.02 g along the Roseau Fault (Fig. 7n), we expect this earthquake to have had limited impact on mass-wasting processes in the study area.

The repeat photomosaic surveys provide further data to support mobilization of debris primarily during earthquakes. We observe little deposition of rubble during the 3.5-year inter-survey period from 2013 to 2017 during which maximum PGA along the Roseau fault were  $<0.01$  g (Figs. 5, 7e). Furthermore, local rubble piles up to  $\sim 1$  m high cover the coseismic ribbon (Fig. 4). Such large rubble piles resulting from continuous mass wasting would imply rapid local erosion rates and widespread evidence of seafloor changes should be documented by the photomosaics from 2013 and 2017. Hence, while we lack pre-seismic observations and we cannot quantify coseismic versus postseismic erosion and deformation, the visual observations

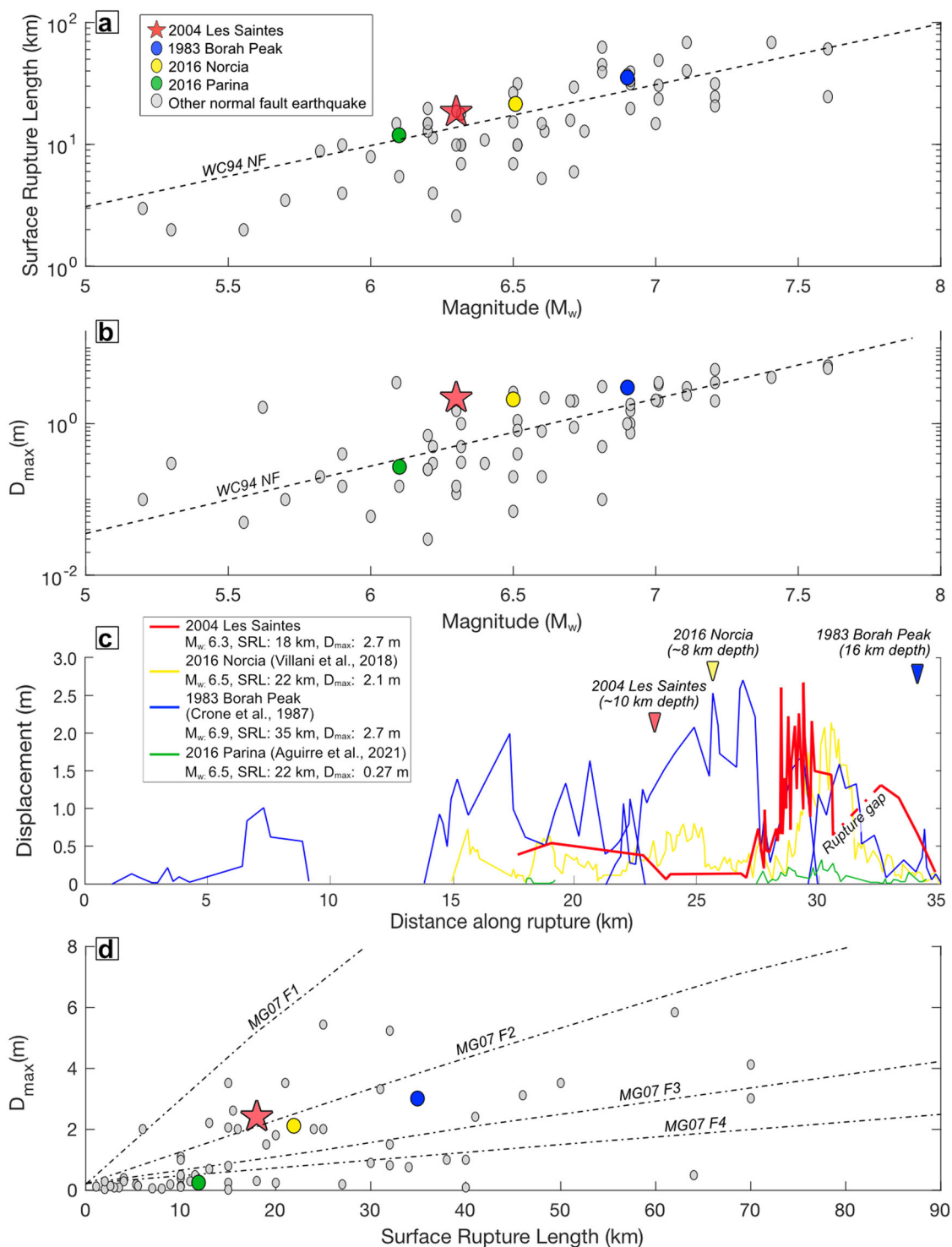


**Fig. 6 Rupture profile comparison and scaling relationships.** **a, b** Log-linear plots of earthquake surface rupture parameters for normal faults. **a** Surface rupture length (SRL) versus magnitude and **b** maximum displacement ( $D_{max}$ ) versus magnitude. The 2004 Les Saintes earthquake is the only submarine datapoint. The dashed line is the regression for normal fault from ref. <sup>1</sup> (WC94 NF). **c** Comparison of the 2004 Les Saintes earthquake surface rupture with the surface rupture profile from other well-studied normal fault earthquakes. Triangles show location of earthquake epicenters. **d**  $D_{max}$  versus SRL for normal fault earthquakes. The dot-dash lines represent optimal fits for different values of stress drop and widths of the seismogenic zone for increasing numbers of ruptured fault segments (F1–F4) from ref. <sup>55</sup> (MG07). Earthquake data is provided in Supplementary Data 6.

combined with modeled PGA are consistent with a hypothesis that local mass wasting of coarse debris is seismically triggered, and that inter- and post-seismic mass wasting is negligible.

These repeat observations also suggest that processes that are continuous and unrelated to seismicity like weathering, alteration,

or abrasion by currents operate at slow rates relative to seismically triggered mass wasting. We acknowledge that our repeat surveys only cover 3.5 years of the 14-year period from the 2004 earthquake to the SUBSAINTES cruise in 2017. It is possible that non-seismic processes trigger punctuated events that were



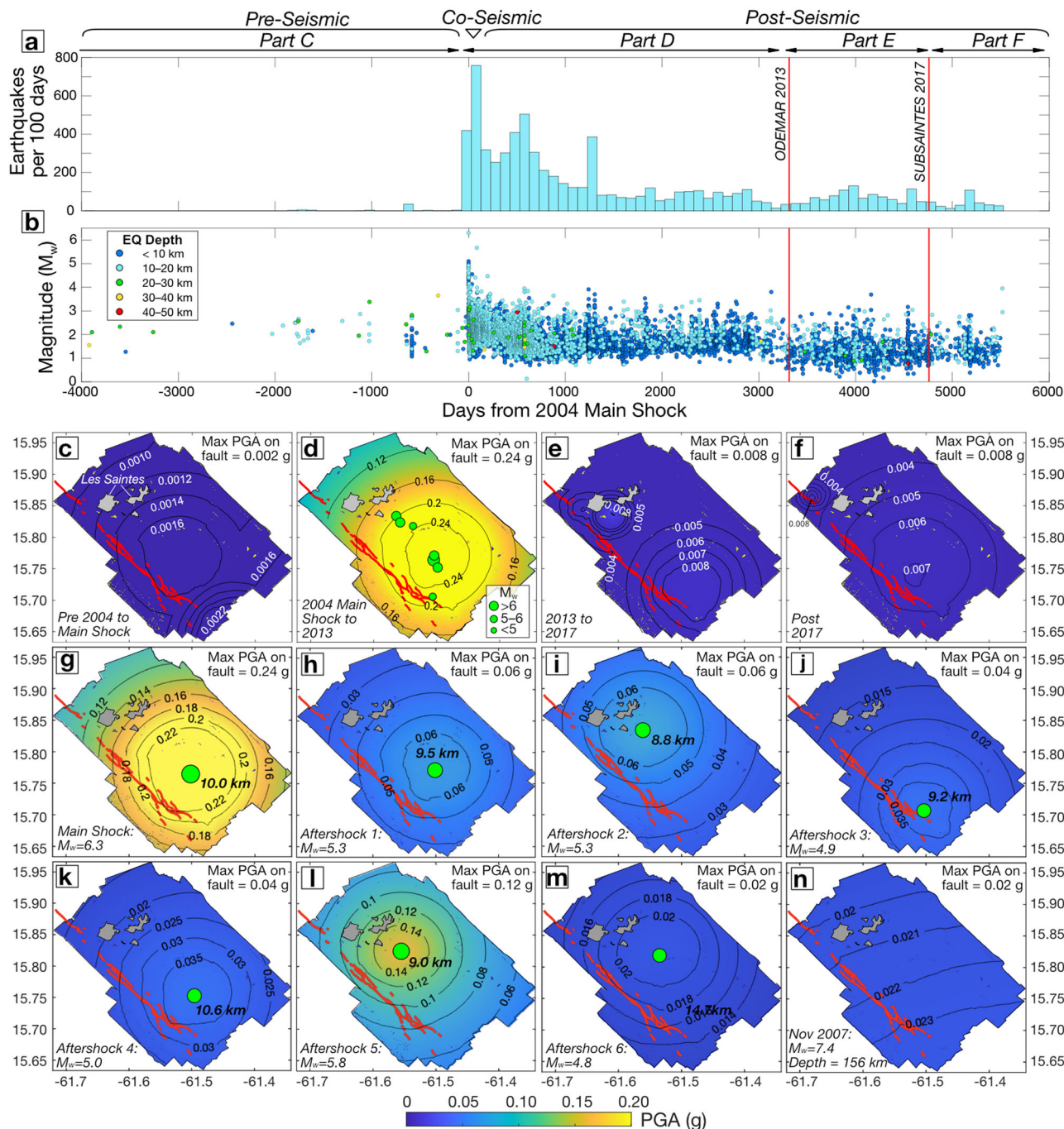


**Fig. 7** Seismicity data and maps of peak ground accelerations (PGA). **a** Frequency of earthquakes per 100 days spanning 4000 days prior to the  $M_w$  6.3 2004 Les Saintes earthquake on 21st November 2004 to 5500 days after the earthquake. **b** The evolution of earthquake magnitude with time for the earthquakes in part A. **c-f** Maps of maximum PGA along the Roseau fault (red line) over certain periods defined by the 2004 earthquake and subsequent cruises. The green circles show the epicenter of the  $M_w$  6.3 2004 main shock and the six largest aftershocks<sup>3</sup>. The thin black lines are PGA contours. PGA are based on the location, depth, and magnitude of all earthquakes shown in part (b) and calculations employed a local ground motion predictive equation<sup>71</sup>. **g-n** Maps of maximum PGA on the Roseau fault for the 2004 main shock and the six largest aftershocks plus a  $M_w$  7.4 earthquake in 2007 offshore from Martinique. Earthquake data are presented in Supplementary Data 8.

not recorded in between the 2013 and 2017 surveys. However, we speculate that these long-term processes more likely act to weaken the bedrock and facilitate failure which occurs primarily when shaken during earthquakes.

The suggestion that bedrock mass wasting on the uplifting footwall is triggered mainly by earthquakes is supported by on-land observations. In the Lesser Antilles, physical erosion is driven mainly by discrete landslides that occur during frequent tropical

storms<sup>62</sup>. To a lesser extent, earthquakes also trigger mass wasting and the 2004 main shock triggered coseismic landslides on the Les Saintes islands<sup>3</sup>. However, even though the region features some of the fastest subaerial weathering rates in the world, landslides are largely inhibited during dry periods<sup>62</sup>. This indicates that on annual–decadal timescales, even when strongly altered by intense weathering, the local volcanic bedrock needs external forcing to induce mass wasting. As the Roseau fault scarp is not subject to

storm-driven erosion, the most plausible external trigger for mass wasting is ground accelerations during earthquakes. Consequently, while mass wasting between 2004 and 2013 cannot be ruled out, we favor a model where the primary geomorphic agent eroding the uplifting footwall is seismic shaking.

Our analysis indicates that mass wasting of well-consolidated basement bedrock along the Roseau fault is triggered by horizontal PGA of at least 0.12 g, and possibly up to 0.24 g. One recent example, based on repeat bathymetry from before and after the  $M_w$  7.8 Kaikōura earthquake in New Zealand, indicates that PGA of 0.38–0.44 g are required to trigger mass wasting in sediments on the continental slope<sup>26,27</sup>. The tectonic setting of the Kaikōura earthquake is clearly different from the Les Saintes earthquake and the Kaikōura rupture was complex and reactivated primarily strike-slip faults<sup>63</sup>. Nevertheless, a comparatively low-triggering threshold in volcanic bedrock on the Roseau fault is an interesting comparison.

Morphological parameters from the Roseau fault scarp are indicative of high-strength bedrock. The average slope of the Roseau segment is 20–40° and the slope of the free face averages 72° for heights up to 50 m<sup>30</sup>. These morphological parameters are in contrast to a comparatively low triggering threshold, which should inhibit the preservation of widespread, high-slope surfaces. An explanation for this apparent contradiction is the existence of a threshold height, above which the steep scarp becomes unstable and prone to erosion via mass wasting. The threshold height could be controlled by gradual weakening of the bedrock over time due to seismic shaking and weathering from seawater. For the Roseau fault scarp, the threshold height is thought to be between 20 and 50 m<sup>30</sup>. We suggest it is the prevalence of high-slope scarps above the threshold instability height on the footwall of the Roseau fault that account for a low triggering threshold by rendering the scarp susceptible to gravitational failure and mass wasting during earthquakes.

Indeed, along the continental slope of the Pacific northwest offshore from the USA and Canada, mass wasting is more widespread in older, well-consolidated sediments at the base of the slope compared to younger, less-consolidated sediments on the upper slopes<sup>64–66</sup>. More widespread failure of lower slope sediments can be partially attributed to seismic strengthening in unconsolidated upper slope sediments<sup>65</sup> or local site effects<sup>67</sup>, but the steepness of sediments towards the base of the continental slope is also thought to be an important factor<sup>64</sup>. Observations from the continental slope, despite involving sediments instead of bedrock along the Roseau fault, are consistent with triggering thresholds in submarine basement bedrock being relatively low due to widespread high-slope surface that are above a threshold stability height and, therefore, prone to erosion via gravitational mass wasting during earthquakes.

## Conclusion

We present the first comprehensive coseismic rupture profile for a submarine normal fault based on near-bottom bathymetry data, video imagery, and 3D-terrain models from the Roseau fault and the 2004  $M_w$  6.3 Les Saintes earthquake. We record a northwest-skewed rupture profile with 18 km of coseismic rupture, maximum vertical displacement of 2.7 m, and average coseismic vertical displacement of 0.6 m. The surface rupture and rupture parameters from the submarine Les Saintes earthquake superficially resemble examples of terrestrial normal fault surface ruptures for similar magnitudes. This work demonstrates the novel application of underwater vehicles to undertake submarine paleoseismic or rapid response studies and provides a methodological blueprint for future studies to map and quantify submarine coseismic ruptures. Further submarine rupture studies

will also improve the applicability of scaling relationships for submarine faults and validate geophysical inversion models, which provide important inputs for models of tsunami hazard or stress transfer. Our approach has certain drawbacks because we cannot precisely determine the proportion of observed rupture length and displacement attributable to the 2004 main shock, the largest aftershocks, or post-seismic deformation, nor the width of the damage zone. Consequently, further examples of systematic and comprehensive submarine rupture characterization are required to compare the surface rupture propagation between submarine and subaerial faults.

We also document local mass wasting features covering the coseismic rupture and use repeat seafloor surveys along with maps of peak ground accelerations (PGA) to investigate mass wasting triggering thresholds in well-consolidated basement. We suggest a triggering threshold in basement bedrock for PGA of ~0.1–0.2 g. This relatively low triggering threshold may be attributed to the abundance of steep scarps in the footwall of the Roseau fault, which are above a threshold stability height and therefore inherently unstable and susceptible to gravitational failure via mass wasting. Triggering thresholds for mass wasting provide an important data point for mass wasting triggers in strong bedrock, which is vital for studies linking submarine earthquakes with landslides and tsunamis. Seismic triggering of mass wasting is also an important process that shapes seafloor landscapes e.g., abyssal hills which cover large parts of the seafloor. However, additional observations linking earthquake ruptures to mass wasting are required to characterize what is a complex relationship due to the numerous factors involved (e.g., lithology, rock strength, slope).

## Methods

**Research cruises.** We collected the main photographic, bathymetric, and video datasets analyzed for this study during the 2017 SUBSAINTES cruise onboard the research vessel L'Atalante<sup>34</sup>. Data from the SUBSAINTES cruise was supplemented by further photographic, bathymetric, and video datasets from the 2013 ODEMAR cruise conducted onboard the research vessel Pourquoi pas?<sup>33</sup> and by ship-based multibeam bathymetry data obtained during the 2010 BATHYSAINTES cruise, also conducted onboard the research vessel Pourquoi pas?<sup>68</sup>. A summary of the datasets used in this study is included in Supplementary Data 9.

**Bathymetry data.** During the SUBSAINTES cruise, we collected near-bottom, high-resolution bathymetry data using the AUV Aster<sup>x</sup> (IFREMER, France), equipped with a Kongsberg Reson SMF EM2040. The AUV surveyed at ~70 m above the seafloor, covering ~100 km<sup>2</sup> of seafloor between Les Saintes and Dominica (Fig. 1a). The AUV data were processed using the CARAIBES (IFREMER) and gridded to produce digital terrain models (DTMs) with a 1-m cell size. AUV bathymetry was also acquired by AUV Abyss (GEOMAR) during the ODEMAR cruise and the resulting DTM was gridded with a 2-m cell size. Ship-based multibeam bathymetry data was obtained during the 2010 BATHYSAINTES cruise using a 0.5° × 0.5° beam width multibeam echosounder (Reson Seabat 7150 at 24 kHz). The resulting bathymetry provides continuous seafloor coverage across the study area and allows gridding of a DTM with a 10-m cell size (Fig. 1b; see details in refs. <sup>13,69</sup>).

**ROV seafloor photomosaics.** We collected still-camera images of the seafloor for each dive from the 2013 ODEMAR cruise and the 2017 SUBSAINTES cruise using vertically mounted cameras on the ROV Victor6000 (IFREMER, France). The georeferenced photomosaics have an approximate horizontal resolution of 1 cm and provide systematic surveys of various sections of the Roseau fault. Images from the ODEMAR cruise are black and white, while those from SUBSAINTES are in color. We built navigated photomosaics<sup>70</sup> from images acquired in transits at ~5 m above the seafloor in specific areas of interest and images were processed for feature matching and blending.

**ROV 3D terrain models from video imagery.** During the SUBSAINTES and ODEMAR cruises, we collected video imagery at multiple locations along the Roseau fault scarp (Fig. 1c) using a Sony FCB-H11 high-definition video camera mounted on a pan-and-tilt platform at the front of ROV Victor6000. We surveyed using overlapping tracks at speeds of <0.5 m/s and at distances of ~2–5 m from outcrop surfaces. Extracted video frames were corrected for distortion, illumination, equalized, and color-shifted prior to processing using structure-from-motion

techniques to create three-dimensional terrain models of each outcrop<sup>70</sup>. All models are texture-mapped, scaled, and georeferenced to facilitate visualization for geological interpretations and provide proper scaling for quantitative studies with model resolutions of ~1 cm or better<sup>35,36</sup>.

**Measurements of vertical displacement: 3D models.** We visually inspected individual 3D models and digitized markers of coseismic displacement. These include the top and bottom of coseismic ribbons on either the fault free face, if present on freshly exposed basement scarps, or the top and bottom of faults and fissures rupturing through rubble and sediment. Uncertainties are estimated from several individual measurements made along each image of the rupture and we report the average value with one standard deviation uncertainty in each case. 3D models may include one or more digitized ruptures, and we reported the averaged value from an outcrop if multiple measurements were made at the same outcrop. Displacements of individual rupture sections and the average for each model are provided in Supplementary Data 2.

**Measurements of vertical displacement: laser scalars.** Four parallel lasers mounted on ROV Victor6000 define a square of 16.5 cm per side. The projected beams, visible on the ROV HD video imagery, provide scaling that can be exploited to scale 3D models and estimate the size of features and the vertical coseismic displacement along the Roseau fault<sup>35,36</sup>. The distance between the parallel laser beams in the images depends on the orientation and geometry of the outcrop surface relative to that of the laser beams, and surfaces at a high angle from the image will have large uncertainty. For optimal laser measurements, we selected video frames that contained visible laser beams with imaging sub-perpendicular to the outcrop. From these frames, we digitized the top and bottom of coseismic features at several positions in each image to obtain an average value and an estimate of the associated error (Supplementary Fig. 4; Supplementary Data 3). At selected positions, we compared displacements evaluated from laser scalar imagery with those from 3D terrain models and the results are consistent and within the estimated errors.

**Seismicity data.** For the  $M_w$  6.3 2004 main shock and the six largest aftershocks, we used the relocated earthquake locations and magnitudes from ref. <sup>3</sup>. For regional seismicity prior to the 2004 main shock, we used data from the Centre de Données Sismologiques des Antilles catalog, which represents an ongoing attempt to create an integrated database of the various earthquake catalogs from the Lesser Antilles<sup>60</sup>. For the period covering and following the 2004 Les Saintes earthquake, but not including the 2004 main shock and the six largest aftershocks, we assembled earthquake data from the seismic catalog generated by the Institut de Physique du Globe de Paris, which manages two volcanological and seismological observatories in Martinique and Guadeloupe. From this combined catalog, we excluded earthquakes deeper than 50 km and associated with the subducting plate interface, and those outside our study area (15.95–15.65°N and –61.7 to –61.4°W). The final combined dataset contained 7356 earthquakes recorded over ~9500 days up to November 2019 (Fig. 7, Supplementary Fig. 3).

**Maps of peak ground accelerations.** We calculated PGA using the ground motion predictive equation (GMPE) from for Les Saintes<sup>71</sup>. The GMPE takes the form:

$$\log(PGA) = aM + bR - \log(R) + c \quad (1)$$

where  $PGA$  has units of acceleration scaled to gravity ( $g$ ),  $M$  is earthquake magnitude, and  $R$  is hypocentral distance in km. The parameters  $a$ ,  $b$ , and  $c$  are constants calculated locally (0.61755, 0.0030746, and –3.3968, respectively)<sup>71</sup>. For the 7356 earthquakes in the combined seismicity catalog described above, we used the GMPE in Eq. (1) and the earthquake location and magnitude from the earthquake catalogs to calculate maximum horizontal PGA in each cell of the regional 10 m/pixel DTM (Fig. 7). We present maps of the maximum PGA for each cell of the DTM over specific time periods and for the main shock and six largest aftershocks in Fig. 7.

## Data availability

A 25-m per cell version of the regional bathymetry data from the BATHYSAINTES cruise is available at <https://doi.org/10.17882/8117472>. The 1-m per cell AUV-bathymetry data from the SUBSAINTES cruise is available at <https://doi.org/10.17882/7989573> and ROV-navigation files from the SUBSAINTES cruise are available at <https://doi.org/10.17882/8229074>. ROV dive footage from the SUBSAINTES cruise is available at <https://video.ifremer.fr/>. Video-derived 3D terrain models along the Roseau fault are available from <https://doi.org/10.17882/8424975>. Photomosaics from the ODEMAR cruise are available at <https://doi.org/10.17882/9524376> and photomosaics from the SUBSAINTES cruise are available at <https://doi.org/10.17882/9524277>. Full details of all datasets used in the study are summarized in Supplementary Data 9 which is available along with all other supplementary tables referenced in this work from <https://doi.org/10.6084/m9.figshare.2330415878>.

Received: 1 September 2022; Accepted: 3 July 2023;

Published online: 22 July 2023

## References

- Wells, D. L. & Coppersmith, K. J. New empirical relationships among magnitude, rupture length, rupture width, rupture area, and surface displacement. *Bull. Seismol. Soc. Am.* **84**, 974–1002 (1994).
- Leonard, M. Earthquake fault scaling: self-consistent relating of rupture length, width, average displacement, and moment release. *Bull. Seismol. Soc. Am.* **100**, 1971–1988 (2010).
- Feuillet, N. et al. The  $M_w = 6.3$ , November 21, 2004, Les Saintes earthquake (Guadeloupe): tectonic setting, slip model and static stress changes. *J. Geophys. Res.: Solid Earth* **116**, 1–25 (2011).
- Moreno, M. S., Bolte, J., Klotz, J. & Melnick, D. Impact of megathrust geometry on inversion of coseismic slip from geodetic data: application to the 1960 Chile earthquake. *Geophys. Res. Lett.* **36**, L16310 (2009).
- Mildon, Z. K., Roberts, G. P., Faure Walker, J. P. & Iezzi, F. Coulomb stress transfer and fault interaction over millennia on non-planar active normal faults: the  $M_w$  6.5–5.0 seismic sequence of 2016–2017, central Italy. *Geophys. J. Int.* **210**, 1206–1218 (2017).
- Mildon, Z. K., Toda, S., Faure Walker, J. P., and Roberts, G. P. Evaluating models of Coulomb stress transfer: Is variable fault geometry important? *Geophys. Res. Lett.* **43**, 12407–12414 (2016).
- Hughes, A. et al. Three-dimensional structure, ground rupture hazards, and static stress models for complex nonplanar thrust faults in the Ventura basin, southern California. *J. Geophys. Res. Solid Earth* **125**, e2020B019539 (2020).
- Fujiwara, T. et al. The 2011 Tohoku-Oki earthquake: displacement reaching the trench axis. *Science* **334**, 1240–1240 (2011).
- Armijo, R. et al. Submarine fault scarps in the Sea of Marmara pull-apart (North Anatolian Fault): implications for seismic hazard in Istanbul. *Geochem. Geophys. Geosyst.* **6**, 1–29 (2005).
- Escartin, J. et al. First direct observation of coseismic slip and seafloor rupture along a submarine normal fault and implications for fault slip history. *Earth Planet. Sci. Lett.* **450**, 96–107 (2016).
- Clark, K. J. et al. Highly variable coastal deformation in the 2016  $MW7.8$  Kaikōura earthquake reflects rupture complexity along a transpressional plate boundary. *Earth Planet. Sci. Lett.* **474**, 334–344 (2017).
- Brodsky, E. E. & Kanamori, H. Elastohydrodynamic lubrication of faults. *J. Geophys. Res.* **106**, 16357–16374 (2001).
- Leclerc, F., Feuillet, N. & Deplus, C. Interactions between active faulting, volcanism, and sedimentary processes at an island arc: insights from Les Saintes channel, Lesser Antilles arc. *Geochem. Geophys. Geosyst.* **17**, 2781–2802 (2016).
- Cordrie, L., Gailler, A., Escartin, J., Feuillet, N. & Heinrich, P. Simulation of the 2004 tsunami of Les Saintes in Guadeloupe (Lesser Antilles) using new source constraints. *Nat. Hazards* **103**, 2103–2129 (2020).
- Hébert, H. et al. The 15 August 2007 Peru earthquake and tsunami: Influence of the source characteristics on the tsunami heights. *Tsunami science four years after the 2004 Indian Ocean Tsunami: Part II: Observation and Data Analysis*, Vol. 166, 211–232 (2009).
- Løvholt, F. et al. Stochastic analysis of tsunami runup due to heterogeneous coseismic slip and dispersion. *J. Geophys. Res. Oceans* **117**, 1–17 (2012).
- Heinrich, P., Schindele, F., Guibourg, S. & Ihmlé, P. F. Modeling of the February 1996 Peruvian Tsunami. *Geophys. Res. Lett.* **25**, 2687–2690 (1998).
- Locat, J. & Lee, H. J. Submarine landslides: advances and challenges. *Can. Geotech. J.* **39**, 193–212 (2002).
- Hampton, M. A., Lee, H. J. & Locat, J. Submarine landslides. *Rev. Geophys.* **34**, 33–59 (1996).
- Lee, H. J. et al. Submarine mass movements on continental margins. In: *Continental Margin Sedimentation: From Sediment Transport to Sequence Stratigraphy* (37, 213–274). Malden: Blackwell Publishing (2007).
- Meunier, P., Hovius, N. & Haines, A. J. Regional patterns of earthquake-triggered landslides and their relation to ground motion. *Geophys. Res. Lett.* **34**, L20408 (2007).
- Owen, L. A. et al. Landslides triggered by the 8 October 2005 Kashmir earthquake. *Geomorphology* **94**, 1–9 (2008).
- Moernaut, J. et al. Giant earthquakes in South-Central Chile revealed by Holocene mass-wasting events in Lake Puyehue. *Sediment. Geol.* **195**, 239–256 (2007).
- Moernaut, J. et al. Lacustrine turbidites as a tool for quantitative earthquake reconstruction: new evidence for a variable rupture mode in south central Chile. *J. Geophys. Res. Solid Earth* **119**, 1607–1633 (2014).
- Ten Brink, U. S., Lee, H. J., Geist, E. L. & Twichell, D. Assessment of tsunami hazard to the U.S. East Coast using relationships between submarine landslides and earthquakes. *Mar. Geol.* **264**, 65–73 (2009).

26. Mountjoy, J. J. et al. Earthquakes drive large-scale submarine canyon development and sediment supply to deep-ocean basins. *Sci. Adv.* **4**, eaar3748 (2018).
27. Howarth, J. D. et al. Calibrating the marine turbidite palaeoseismometer using the 2016 Kaikōura earthquake. *Nat. Geosci.* **14**, 161–167 (2021).
28. Goldfinger, C., Nelson, C. H. & Johnson, J. E., and The Shipboard Scientific Party. Holocene earthquake records from the Cascadia Subduction Zone and Northern San Andreas fault based on precise dating of offshore turbidites. *Annu. Rev. Earth Planet. Sci.* **31**, 555–577 (2003).
29. Macdonald, K. C. Mid-ocean ridges: fine scale tectonic, volcanic and hydrothermal processes within the plate boundary zone. *Annu. Rev. Earth Planet. Sci.* **10**, 155–190 (1982).
30. Hughes, A. et al. Quantification of gravitational mass wasting and controls on submarine scarp morphology along the Roseau fault, Lesser Antilles. *J. Geophys. Res. Earth Surf.* **126**, e2020JF005892 (2021).
31. Bazin, S. et al. The 2004–2005 Les Saintes (French West Indies) seismic aftershock sequence observed with ocean bottom seismometers. *Tectonophysics* **489**, 91–103 (2010).
32. Salichon, J., Lemoine, A. & Aochi, H. Validation of teleseismic inversion of the 2004 Mw 6.3 Les Saintes, Lesser Antilles, earthquake by 3D finite-difference forward modeling. *Bull. Seismol. Soc. Am.* **99**, 3390–3401 (2009).
33. Escartin, J. and Andreani, M. ODEMAR cruise, RV Pourquoi pas? <https://doi.org/10.17600/13030070>.
34. Escartin, J., Le Friant, A. and Feuillet, N. SUBSAINTES cruise, RV L'Atalante. <https://doi.org/10.17600/17001000> (2017).
35. Istenič, K., Gracías, N., Arnaubec, A., Escartin, J. & Garcia, R. Automatic scale estimation of structure from motion-based 3D models using laser scalars in underwater scenarios. *ISPRS J. Photogr. Remote Sens.* **159**, 13–25 (2020).
36. Istenič, K., Gracías, N., Arnaubec, A., Escartin, J. & Garcia, R. Scale accuracy evaluation of image-based 3D reconstruction strategies using laser photogrammetry. *Remote Sens.* **11**, 2093 (2019).
37. Henri, M. et al. K-Ar Geochronology and geochemistry of underwater lava samples from the Subsaintes cruise offshore Les Saintes (Guadeloupe): insights for the Lesser Antilles arc magmatism. *Mar. Geol.* **450**, 106862 (2022).
38. Brozzetti, F. et al. High-resolution field mapping and analysis of the August–October 2016 coseismic surface faulting (central Italy earthquakes): slip distribution, parameterization, and comparison with global earthquakes. *Tectonics* **38**, 417–439 (2019).
39. Villani, F. et al. Surface faulting of the 30 October 2016  $M_w$  6.5 Central Italy earthquake: detailed analysis of a complex coseismic rupture. *Tectonics* **37**, 3378–3410 (2018).
40. Avar, B. B. & Hudyma, N. W. Earthquake surface rupture: a brief survey on interdisciplinary research and practice from geology to geotechnical engineering. *Rock. Mech. Rock. Eng.* **52**, 5259–5281 (2019).
41. Sibson, R. H. Thickness of the seismic slip zone. *Bull. Seismol. Soc. Am.* **93**, 1169–1178 (2003).
42. Kozdon, J. E. & Dunham, E. M. Rupture to the trench: dynamic rupture simulations of the 11 March 2011 Tohoku earthquake. *Bull. Seismol. Soc. Am.* **103**, 1275–1289 (2013).
43. Cappa, F., Perrin, C., Manighetti, I. & Delor, E. Off-fault long-term damage: a condition to account for generic, triangular earthquake slip profiles. *Geochem. Geophys. Geosyst.* **15**, 1476–1493 (2014).
44. Manighetti, I., King, G. & Sammis, C. G. The role of off-fault damage in the evolution of normal faults. *Earth Planet. Sci. Lett.* **217**, 399–408 (2004).
45. Delorme, A. et al. Complex deformation at shallow depth during the 30 October 2016  $M_w$  6.5 Norcia earthquake: interference between tectonic and gravity processes? *Tectonics* **39**, e2019TC005596 (2020).
46. Crone, A. J. et al. Surface faulting accompanying the Borah Peak earthquake and segmentation of the lost river fault, central Idaho. *Bull. Seismol. Soc. Am.* **77**, 739–770 (1987).
47. Bello, S. et al. High-detail fault segmentation: deep insight into the anatomy of the 1983 Borah Peak Earthquake rupture zone (Mw 6.9, Idaho, USA). *Lithosphere* **2022**, 8100224 (2022).
48. DuRoss, C. B. et al. Fault segmentation: new concepts from the Wasatch Fault Zone, Utah, USA. *J. Geophys. Res. Solid Earth* **121**, 1131–1157 (2016).
49. Crone, A. J. & Haller, K. M. Segmentation and the coseismic behavior of Basin and Range normal faults: examples from east-central Idaho and southwestern Montana, U.S.A. *J. Struct. Geol.* **13**, 151–164 (1991).
50. Klinger, Y. High-resolution satellite imagery mapping of the surface rupture and slip distribution of the Mw 7.8, 14 November 2001 Kokoxili Earthquake, Kunlun Fault, Northern Tibet, China. *Bull. Seismol. Soc. Am.* **95**, 1970–1987 (2005).
51. Iezzi, F. et al. Coseismic throw variation across along-strike bends on active normal faults: implications for displacement versus length scaling of earthquake ruptures. *J. Geophys. Res. Solid Earth* **123**, 9817–9841 (2018).
52. Manighetti, I., King, G. C. P., Gaudemer, Y., Scholz, C. H. & Doubre, C. Slip accumulation and lateral propagation of active normal faults in Afar. *J. Geophys. Res.* **106**, 13667–13696 (2001).
53. Ferrario, M. F. & Livio, F. Characterizing the distributed faulting during the 30 October 2016, Central Italy Earthquake: a reference for fault displacement hazard assessment. *Tectonics* **37**, 1256–1273 (2018).
54. Perrin, C., Manighetti, I., Ampuero, J.-P., Cappa, F. & Gaudemer, Y. Location of largest earthquake slip and fast rupture controlled by along-strike change in fault structural maturity due to fault growth. *J. Geophys. Res. Solid Earth* **121**, 3666–3685 (2016).
55. Manighetti, I., Campillo, M., Bouley, S. & Cotton, F. Earthquake scaling, fault segmentation, and structural maturity. *Earth Planet. Sci. Lett.* **253**, 429–438 (2007).
56. Bloom, C. K., Howell, A., Stahl, T., Massey, C. & Singeisen, C. The influence of off-fault deformation zones on the near-fault distribution of coseismic landslides. *Geology*. **50**, 272–277 (2022).
57. Abrahamson, N. A. & Silva, W. J. Empirical response spectral attenuation relations for shallow crustal earthquakes. *Seismol. Res. Lett.* **68**, 94–127 (1997).
58. Ambraseys, N. N., Douglas, J., Sarma, S. K. & Smit, P. M. Equations for the estimation of strong ground motions from shallow crustal earthquakes using data from Europe and the Middle East: horizontal peak ground acceleration and spectral acceleration. *Bull. Earthq. Eng.* **3**, 1–53 (2005).
59. Douglas, J. Earthquake ground motion estimation using strong-motion records: a review of equations for the estimation of peak ground acceleration and response spectral ordinates. *Earth-Sci. Rev.* **61**, 43–104 (2003).
60. Bengoubou-Valerius, M., Bazin, S., Bertil, D., Beauducel, F. & Bosson, A. CDSA: a new seismological data center for the French Lesser Antilles. *Seismol. Res. Lett.* **79**, 90–102 (2008).
61. Yuan, R. M. et al. Density distribution of landslides triggered by the 2008 wenchuan earthquake and their relationships to peak ground acceleration. *Bull. Seismol. Soc. Am.* **103**, 2344–2355 (2013).
62. Rad, S., Rivé, K., Vittecoq, B., Cerdan, O. & Allègre, C. J. Chemical weathering and erosion rates in the lesser antilles: an overview in Guadeloupe, Martinique and Dominica. *J. South Am. Earth Sci.* **45**, 331–344 (2013).
63. Hamling, I. J. et al. Complex multifault rupture during the 2016  $M_w$  7.8 Kaikōura earthquake, New Zealand. *Science*. **356**, eam7194 (2017).
64. Hill, J. C., Watt, J. T. & Brothers, D. S. Mass wasting along the Cascadia subduction zone: implications for abyssal turbidite sources and the earthquake record. *Earth Planet. Sci. Lett.* **597**, 117797 (2022).
65. Greene, H. G. et al. Slope failure and mass transport processes along the Queen Charlotte Fault Zone, western British Columbia. *Geol. Soc.* **477**, 85–106 (2019). London, Special Publications.
66. Brothers, D. S. et al. Slope failure and mass transport processes along the Queen Charlotte Fault, southeastern Alaska. *Geol. Soc.* **477**, 69–83 (2019). London, Special Publications.
67. Gomberg, J. Cascadia onshore-offshore site response, submarine sediment mobilization, and earthquake recurrence. *J. Geophys. Res. Solid Earth* **123**, 1381–1404 (2018).
68. Deplus, C. and Feuillet, N. BATHYSAINTES cruise, RV Pourquoi pas? <https://doi.org/10.17600/10030020> (2010).
69. Leclerc, F. et al. The Holocene drowned reef of Les Saintes plateau as witness of a long-term tectonic subsidence along the Lesser Antilles volcanic arc in Guadeloupe. *Mar. Geol.* **355**, 115–135 (2014).
70. Campos, R., Garcia, R., Alliez, P. & Yvinec, M. A surface reconstruction method for in-detail underwater 3D optical mapping. *Int. J. Robot. Res.* **34**, 64–89 (2015).
71. Beauducel, F. et al. Empirical model for rapid macroseismic intensities prediction in Guadeloupe and Martinique. *Comptes Rendus Geosci.* **343**, 717–728 (2011).
72. Deplus, C. & Feuillet, N. Bathymetry from Les Saintes area (Lesser Antilles volcanic arc): 25 m grid from the Bathysaintes cruise. Seanoé. <https://doi.org/10.17882/81174> (2021).
73. Leclerc, F. et al. SUBSAINTES AUV AsterX Bathymetry and backscatter (1 m resolution). Seanoé. <https://doi.org/10.17882/79895> (2023).
74. Escartin, J. SUBSAINTES 2017 ROV Victor tracks—renavigated data for ROV dives. Seanoé. <https://doi.org/10.17882/82290> (2021).
75. Escartin, J., Arnaubec, A., Gracías, N. & Istenič, K. 3D textured models of the along the Roseau Fault scarp between Les Saintes and Dominica (Lesser Antilles): seafloor rupture of the 2004  $M_w$  6.3 Les Saints earthquake. *Seanoé* <https://doi.org/10.17882/84249> (2017).
76. Escartin, J., Gracías N. & Garcia, R. ODEMAR cruise: ROV Victor photomosaics—French Antilles—GEOTIFFS (blended & renavigated, UTM 20N). Seanoé. <https://doi.org/10.17882/95243>(2023).
77. Escartin, J., Gracías N. & Garcia, R. SUBSAINTES Cruise—ROV VICTOR photomosaics, French Antilles—GEOTIFFS (navigation-based mosaics, no matching, UTM20N). Seanoé. <https://doi.org/10.17882/95242> (2023).
78. Hughes, A. et al. Seafloor coseismic ruptures and mass wasting from the 2004  $M_w$  6.3 Les Saintes submarine earthquake: Supplementary Tables. Figshare. <https://doi.org/10.6084/m9.figshare.23304158.v1> (2023).

## Acknowledgements

We are indebted to the crew, officers, engineers, and science parties of the ODEMAR (2013) and SUBSAINTES (2017) cruises, whose tireless work allowed us to acquire the data used in this study. This work is supported by the French Oceanographic Fleet, by ANR project SERSURF (ANR-17-CE31-0020) and from CNRS-INSU System programs. GEOMAR supported AUV operations during the ODEMAR cruise.

## Author contributions

AH: Manuscript writing, data analysis, project design. JE: Manuscript writing, data analysis, project design, data collection. JB: Manuscript editing, data analysis, data collection. FL: Manuscript editing, data analysis, project design, data collection. MA: Manuscript editing, data collection. J-AO: Manuscript editing, data collection. AA: Manuscript editing, data collection. AD: Manuscript editing, data collection. AD: Manuscript editing, data collection. CD: Manuscript editing, data collection. NF: Manuscript editing, project design, data collection. CG: Manuscript editing, data collection. NG: Manuscript editing, data collection. CH: Manuscript editing, data collection. KI: Manuscript editing, data collection. J-CK: Manuscript editing, data collection. ALF: Manuscript editing, data collection. CM: Manuscript editing, data collection. CM: Manuscript editing, data collection. SLO: Manuscript editing, data collection. XQ: Manuscript editing, data collection.

## Competing interests

The authors declare no competing interests.

## Additional information

**Supplementary information** The online version contains supplementary material available at <https://doi.org/10.1038/s43247-023-00919-x>.

**Correspondence** and requests for materials should be addressed to Alex Hughes.

**Peer review information** *Communications Earth & Environment* thanks Danny Brothers, Kiichiro Kawamura and the other, anonymous, reviewer(s) for their contribution to the peer review of this work. Primary Handling Editors: Teng Wang and Joe Aslin. A peer review file is available.

**Reprints and permission information** is available at <http://www.nature.com/reprints>

**Publisher's note** Springer Nature remains neutral with regard to jurisdictional claims in published maps and institutional affiliations.



**Open Access** This article is licensed under a Creative Commons Attribution 4.0 International License, which permits use, sharing, adaptation, distribution and reproduction in any medium or format, as long as you give appropriate credit to the original author(s) and the source, provide a link to the Creative Commons licence, and indicate if changes were made. The images or other third party material in this article are included in the article's Creative Commons licence, unless indicated otherwise in a credit line to the material. If material is not included in the article's Creative Commons licence and your intended use is not permitted by statutory regulation or exceeds the permitted use, you will need to obtain permission directly from the copyright holder. To view a copy of this licence, visit <http://creativecommons.org/licenses/by/4.0/>.

© The Author(s) 2023